

https://dspace.org/

A review of road models for vehicular control

Limebeer, D. J. N.; Warren, E.

2022-05
Taylor and Francis Group
https://hdl.handle.net/10539/49277
Limebeer, D. J. N., & Warren, E. (2023). A review of road models for vehicular control. Vehicle System Dynamics, 61(6), 1449–1475. https://doi.org/10.1080/00423114.2022.2085582

Downloaded from a DSpace repository. https://dspace.org/



Taylor & Francis
Taylor & Francis Group

Vehicle System Dynamics
International Journal of Vehicle Mechanics and Mobility

ISSN: 0042-3114 (Print) 1744-5159 (Online) Journal homepage: www.tandfonline.com/journals/nvsd20

A review of road models for vehicular control

D. J. N. Limebeer & E. Warren

To cite this article: D. J. N. Limebeer & E. Warren (2023) A review of road models for vehicular control, Vehicle System Dynamics, 61:6, 1449-1475, DOI: 10.1080/00423114.2022.2085582

To link to this article: https://doi.org/10.1080/00423114.2022.2085582

© 2022 The Author(s). Published by Informa UK Limited, trading as Taylor & Francis Group

Published online: 12 Jun 2022.

Submit your article to this journal

Article views: 2330

View related articles

View Crossmark data

Citing articles: 13 View citing articles

Full Terms & Conditions of access and use can be found at
https://www.tandfonline.com/action/journalInformation?journalCode=nvsd20

VEHICLE SYSTEM DYNAMICS
2023, VOL. 61, NO. 6, 1449–1475
https://doi.org/10.1080/00423114.2022.2085582

OPEN ACCESS Check for updates

A review of road models for vehicular control

D. J. N. Limebeer [a] and E. Warren [b]

[a]School of Electrical & Information Engineering, University of the Witwatersrand, Johannesburg, South Africa; [b]General Motors, Concord, NC, USA

ABSTRACT

Over the last 25 years a number of road models have been developed for use in a variety of vehicular control problems. These models are important, because they dictate the force-generating capabilities of the tyres, as well as constrain the movement of the vehicle itself. Early road models used two-dimensional (2D) 'flat road' representations, the advantages and deficiencies of which are well understood. Once it became apparent that three-dimensional effects can be important in limit-performance studies, ribbon-based three-dimensional (3D) road models were developed. The large lateral camber variations on highly-banked NASCAR tracks highlighted deficiencies in ribbon-based road representations that required correction. Upgraded models addressing these deficiencies were only developed recently. The purpose of this paper is to review and compare a number of road models – particularly those developed for use in racing studies. Comparative computed results are provided that hight some of the similarities and differences between these models.

ARTICLE HISTORY
Received 1 October 2021
Revised 16 May 2022
Accepted 17 May 2022

KEYWORDS
Kinematics; mathematical methods; mechanics; optimal control; simulation; track models

1. Introduction

A road model is an integral component of any vehicular control problem formulation, because it provides fundamental constraints on the vehicle's motion. Vehicular control studies date back to the 1950s and include such things as minimum lap-time problems in racing, fuel minimisation problems, fuel-usage-constrained problems, fuel-efficient-route planning problems, and the optimal utilisation of the various power sources in hybrid powertrains. In this context both two- and four-wheeled vehicles have been studied extensively. Our focus here is not on vehicular control per se – a review of much of this literature can be found in [1,2] and the references therein. Instead, we will concentrate on the track and road modelling methodologies that have evolved over the last 20 years. We will also discuss the optimisation of road models based on measured data.

The geometry of the road surface has a significant effect on vehicular performance, because the road-surface geometry impacts directly tyre performance. Obvious examples include a reduction in the tyres' force-generating capacity as a vehicle negotiates the summit of a hill, or conversely, their increased force-generating capability for a vehicle driving through a dip. Similar effects occur in relation to cambered corners, with adverse

CONTACT D. J. N. Limebeer david.limebeer@wits.ac.za, david.limebeer@eng.ox.ac.uk

© 2022 The Author(s). Published by Informa UK Limited, trading as Taylor & Francis Group
This is an Open Access article distributed under the terms of the Creative Commons Attribution-NonCommercial-NoDerivatives License (http://creativecommons.org/licenses/by-nc-nd/4.0/), which permits non-commercial re-use, distribution, and reproduction in any medium, provided the original work is properly cited, and is not altered, transformed, or built upon in any way.

camber particularly troublesome at high speed. The road-surface geometry also influences the suspension and aerodynamic behaviour, because the aerodynamic force system is responsive to the gap between the road surface and the underside of the car. With the increased importance of these 3D influences, road-surface models have necessarily become more complex. We aim to discuss the evolution of road models and show how they are related.

The simplest (and most common) road models relate to planar 'flat' roads. In some early work [3], the trajectory tracking problem for robots that move on flat surfaces is studied. This study makes use of intrinsic coordinates to describe the wheel ground-contact point trajectory relative to a reference curve. A driver model within a model-predictive control (MPC) framework that can optimise the trajectory of a vehicle travelling at constant speed in order to maximise progression along a predefined track is described in [4]. The methodology presented is motivated by the need for a computationally efficient environment for studying 'on-the-limit' driving in minimum-lap-time problems. A 'flat-road' track centreline is taken as the reference trajectory, which is defined in a global reference frame. Related work is presented in [5], which in this case focuses on autonomous driving; a flat-road model is employed again.

A two-part 2D real-time autonomous driving motion planner used for path control is presented in [6]. The resulting trajectories are followed by an autonomous vehicle with small path and speed tracking errors achieved. The reference trajectories were designed to be both smooth and continuous.

Minimum-time cornering strategies on different flat-road surfaces, with different transmission layouts are investigated in [7]. In off-road conditions minimum-time manoeuvres are characterised by aggressive, high-drift counter-steering type manoeuvres, which are reminiscent of rally car driving trajectories. Handbrake cornering on flat roads is analysed and simulated in [8], where the optimality of strategies that are widely used in rally car racing are investigated. The optimal 'virtual driver' is shown to mimic real rally driver behaviour when the optimal control cost function includes the lateral deviation from the road's inside boundary. Minimum-time trajectories on tight hairpins employ handbrake cornering techniques, with the car hugging the inside boundary of the track.

A challenging area of research relates to vehicular active safety control system based on the exploitation of differentially flat [9] vehicle models [10]. In this work a nonlinear differential-flatness-based control system that controls the posture of the vehicle during dangerous situations at intersections is studied. A simple planar polynomial yaw angle reference is used to obtain an injury-mitigating broadside-to-broadside type collision.

A flat-road assumption is also used in autonomous racing, with the trajectory control coming from the theory of non-cooperative games [11]. If the Stackelberg cost function is designed to reward the cars for staying ahead at the end of the horizon, blocking strategies result. A simulation study shows that game theory can be used in competitive autonomous racing for two cars – the real-time computation of competitive racing strategies remains an outstanding problem.

An early fore into three-dimensional road modelling is described in [12], where the influence of road banking in vehicle stability control is studied. This is particularly important on treacherous surfaces such as ice and snow. A technique for bank angle estimation is described that can be used in vehicle stability controllers. The effect of road banking

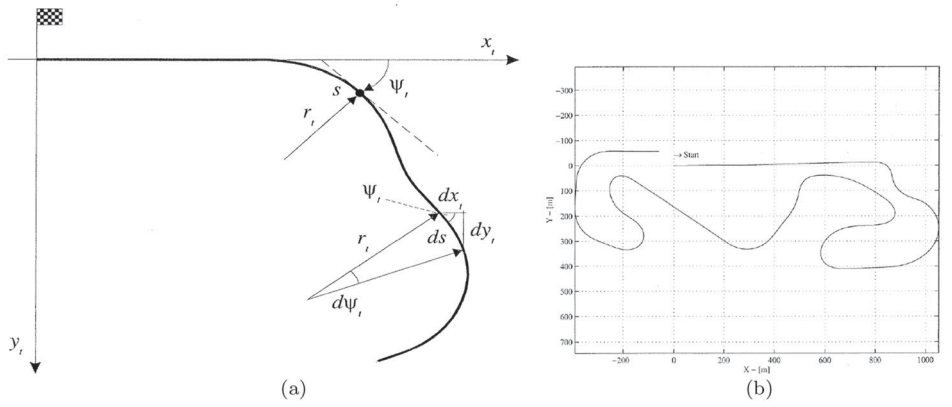


Figure 1. (a) Racing line and notation. (b) Racing line reconstruction with the kinematic model in (2) [21].

disturbances was studied using a bicycle model tailored for banked roads – cornering on inclined surfaces is not considered.

Work relevant to the more advanced aspect 3D rolling contact modelling is described in [13], where the kinematics of the spin-rolling motion of contacting rigid bodies is analysed. This spin-rolling motion formulation is derived in terms of contra-variant vectors, the rolling velocity, and geometric invariants. The effects of the relative curvature and torsion on spin-rolling kinematics are presented. This analysis framework is relevant to the motion planning of machine tools as well as vehicular 3D road modelling.

Curvilinear-coordinate based road descriptions were introduced into the vehicle dynamics literature in [14]. The track closure problem illustrated in Figure 1(b) was solved in the 2D case in [15] by formulating the track-modelling problem as an OCP in which track-closure boundary conditions were introduced. The introduction of closure-related boundary conditions served to 'immunise' the track modelling problem from noise in the survey data as well as integrator drift.

The importance of 3D track models was recognised with the introduction of hybrid power trains into Formula One. Track models of this type are described in [16], in which three track-curvature variables are utilised. Related work that makes use of curvilinear coordinates in 3D road modelling is presented in [17]. The car (represented by a single-track model in this case) is assumed to travel on a local tangent plane under the vehicle. In this framework the car's road position can be tracked by differential equations that are driven by the car's velocity without the need for a tracking algorithm.

Three-dimensional road modelling is also described in the recent paper [18], in which ideas from classical differential geometry are more fully utilised. Citations [16,17] and [18] use several of the same ideas – we will review their similarities and differences. In more recent work, motivated in part by NASCAR oval modelling issues, 3D tracks with significant lateral curvature variations are studied in [19]. The lateral curvature issue is also covered in [20], where the problem is set up in the differential-geometric framework suggested in [18].

Early work on racing line and track reconstruction made use of on-board measurements of the forward speed and the lateral acceleration [21]. The idea is that the cornering radius

of curvature can approximated by

$$r_t \approx \frac{v^2}{a_y}, \tag{1}$$

where v is the forward speed and a_y the lateral acceleration.

Almost unwittingly, (1) introduces the idea of 'curvature' and thus also the introduction of intrinsic coordinate track descriptions.

Using the notation in Figure 1(a), the following relationships are immediate

$$\Psi_t' = 1/r_t; \quad x_t' = \cos\Psi_t; \quad y_t' = \sin\Psi_t; \quad \dot{s} = v, \tag{2}$$

where s is the distance travelled. The primes denote derivatives with respect to s, and a dot denotes a derivative with respect to time. Integrating these equations gives the yaw angle Ψ_t, and the path coordinates x_t and y_t as a function of s. In other words, equations (2) can be used to express the trajectory parameters as functions of the elapsed distance s, which is a convenient replacement for the independent 'time' variable. This change of variable brings with it advantages in the context of vehicular optimal control problems (OCP) [2].

Figure 1(b) shows the outcome of a racing line reconstruction exercise that is based on the kinematic model in (2). Formula One aficionados will recognise Figure 1(b) as an attempt to reconstruct the racing line on the racing circuit in Barcelona, Spain. This preliminary study contains several of the key ideas, and serves to motivate the remainder of the paper. Clearly evident is the fact that measurement noise and integrator drift conspire to prevent the reconstructed racing line from closing on itself. A number of ad-hoc remedies were suggested in an attempt to repair these noise- and integrator-drift related defects [21], with much improved procedures described in [15].

Section 2 contains the notion and background material that will be required in the sequel. Section 3 is largely introductory and covers 2D road models within the formalism used for more advanced models. The OCP used to optimise the track parameters is also outlined. The velocity constraints associated with the 2D model are covered in Section 3.1. These ideas are then extended in Section 4 to the three-dimensional case. Extensions to the model discussed in Section 4 that address local curvature changes are covered in Section 5. The velocity constraints associated with this model are given in Section 5.1. The optimisation of the road parameters in the 3D case is dealt with in Section 6. The classical differential-geometric approach to 3D road modelling is covered in Section 7. The translational and angular velocity constraints are given in Sections 7.1 and 7.2, respectively. The parametrisation of the Darlington Raceway is covered in Section 7.3 – Darlington is a 2.198 km egg-shaped oval that is run in the counter-clockwise direction (left-hand-cornering) [19,20]. Comparative results are given in Section 8, with some conclusions drawn in Section 9.

2. Notion and background

We will require several frames of reference. The inertial and car-fixed reference frames will be denoted $[\boldsymbol{e}_x^g, \boldsymbol{e}_y^g, \boldsymbol{e}_z^g]$ and $[\boldsymbol{e}_x^b, \boldsymbol{e}_y^b, \boldsymbol{e}_z^b]$, respectively; we will also require road-related frames of reference that will be introduced later. If vector $\boldsymbol{q}^b$ is expressed in a rotating frame, then it can also be described in the inertial frame as $\boldsymbol{q}^g = R\boldsymbol{q}^b$ for some orthogonal time-varying

rotation matrix R. If $\frac{\mathrm{d}\boldsymbol{q}}{\mathrm{d}t}$ is the time derivative of a vector, and $\dot{\boldsymbol{q}}$ represents the time derivative of its components, it then follows that:

$$\begin{aligned}\frac{\mathrm{d}\boldsymbol{q}^g}{\mathrm{d}t} &= \dot{R}\boldsymbol{q}^b + R\dot{\boldsymbol{q}}^b \\ &= R(R^T\dot{R})\boldsymbol{q}^b + R\dot{\boldsymbol{q}}^b \quad \text{note: } RR^T = I \\ \Rightarrow \frac{\mathrm{d}\boldsymbol{q}^b}{\mathrm{d}t} &= (R^T\dot{R})\boldsymbol{q}^b + \dot{\boldsymbol{q}}^b,\end{aligned}$$

where $R^T\dot{R}$ is a skew-symmetric matrix representation of the angular velocity vector of the rotating frame. These arguments are developed in detail in Section 26B of [22]. The above arguments lead to the well-know formula

$$\frac{\mathrm{d}\boldsymbol{q}^b}{\mathrm{d}t} = \boldsymbol{\omega}^b \times \boldsymbol{q}^b + \dot{\boldsymbol{q}}^b, \tag{3}$$

in which $\frac{\mathrm{d}\boldsymbol{q}^b}{\mathrm{d}t}$ is the *absolute velocity of* $\boldsymbol{q}^b$ expressed in the body-fixed frame, $\boldsymbol{\omega}^b \times \boldsymbol{q}^b$ is the *transferred velocity of rotation*, (expressed in the body-fixed frame), and $\dot{\boldsymbol{q}}^b$ is the *relative velocity* expressed in the body-fixed frame. It now follows that for each body-fixed basis vector

$$\begin{bmatrix} \frac{\mathrm{d}\boldsymbol{e}_x^b}{\mathrm{d}t} & \frac{\mathrm{d}\boldsymbol{e}_y^b}{\mathrm{d}t} & \frac{\mathrm{d}\boldsymbol{e}_z^b}{\mathrm{d}t} \end{bmatrix} = \begin{bmatrix} 0 & -\omega_z^b & \omega_y^b \\ \omega_z^b & 0 & -\omega_x^b \\ -\omega_y^b & \omega_x^b & 0 \end{bmatrix} \begin{bmatrix} \boldsymbol{e}_x^b & \boldsymbol{e}_y^b & \boldsymbol{e}_z^b \end{bmatrix}. \tag{4}$$

We will be dealing with basis trihedra with origins that traverse parametrised curves. Suppose in Figure 2 that the centre line of a road is described by the parametrised curve

$$\mathcal{C} = \left\{ \boldsymbol{x}_c(s) = \begin{bmatrix} x(s) & y(s) & z(s) \end{bmatrix}^T \in \mathbb{R}^3 : s \in [s_0, s_f] \right\}, \tag{5}$$

in which the Cartesian coordinates are expressed in the inertial reference frame; $x(s)$, $y(s)$ and $z(s)$ are functions of the *arc length* $s \in [s_0, s_f]$. We will assume that each element of $\frac{\mathrm{d}^3\boldsymbol{x}_c}{\mathrm{d}s^3}$ is continuous and that $\frac{\mathrm{d}^2\boldsymbol{x}_c}{\mathrm{d}s^2}$ is not identically zero for any s. A curve is deemed to be *simple*, if any point on the curve corresponds to a single value of s – simplicity in this sense will be assumed in what follows. The vector tangent to the centre line is given by $\boldsymbol{x}_c'(s) = \boldsymbol{t}$; the prime represents a derivative with respect to s; $\boldsymbol{t}$ is a unit vector if s is the arc-length. Since $\boldsymbol{t}.\boldsymbol{t} = 1$, $\boldsymbol{t}'.\boldsymbol{t} = 0$ and so $\boldsymbol{t}'$ is orthogonal to $\boldsymbol{t}$, with $\boldsymbol{x}_c''(s) = \boldsymbol{t}' = \kappa\boldsymbol{p}$. The unit vector $\boldsymbol{p}$ is the *principal normal* to $\mathcal{C}$ and κ the *curvature*. The *binormal* to the curve is the unit vector $\boldsymbol{b}$ defined by the cross product $\boldsymbol{b} = \boldsymbol{t} \times \boldsymbol{p}$. The *torsion* is defined by $\tau = -\boldsymbol{p}.\boldsymbol{b}'$, which describes how the binormal changes in the $\boldsymbol{p}$ direction. The curvature and torsion define the angular velocity the moving trihedron using the *Frenet–Serret* equations [23].

When the moving trihedron is rotated so that its osculating plane is tangent to the road surface at the centre line, a third curvature variable must be introduced. In this event the moving trihedron is the *Darboux frame*. The Darboux frame $\begin{bmatrix} \boldsymbol{t} & \boldsymbol{n} & \boldsymbol{m} \end{bmatrix}$ has spatial angular velocity $\begin{bmatrix} \Omega_x & \Omega_y & \Omega_z \end{bmatrix}$ (in rad/m). In this coordinate system $\boldsymbol{m}$ is normal to the *osculating* plane, $\boldsymbol{n}$ is normal to the *rectifying* plane, while $\boldsymbol{t}$ is normal to the *normal* plane [23,24].

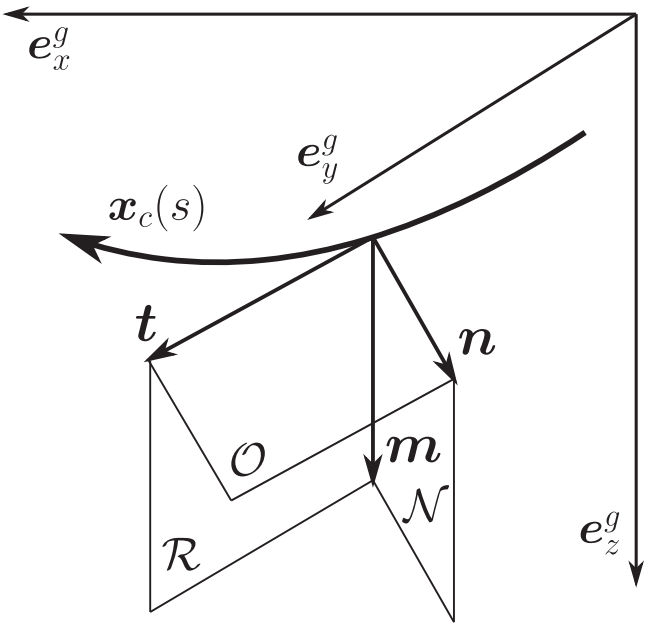


Figure 2. Moving trihedron. Plane $\mathcal{O}$ is the osculating plane, plane $\mathcal{R}$ is the rectifying plane, and plane $\mathcal{N}$ is the normal plane.

Road surfaces and vehicle trajectories will be described in Darboux frame coordinates. We will describe a general road surface by

$$\mathcal{S} = \left\{ \boldsymbol{x}_P(s,n) = \int \boldsymbol{t}\,\mathrm{d}s + \boldsymbol{n}(s)n + \boldsymbol{m}(s)m(s,n) \in \mathbb{R}^3 \,:\, s \in [s_i, s_f],\ n \in \frac{1}{2}[-r_w, r_w] \right\}, \tag{6}$$

in which the parametric variables are s, the distance travelled along the centre line, and n, which is the distance from the track's centre line. Two rather than three independent variables are required, because $\boldsymbol{x}_P(s,n)$ is constrained to the road surface. Following [19,20], we suppose that the road surface is described by $m(s,n)$, which represents height variations perpendicular to the osculating plane of the Darboux frame on the centreline. This is a parametrisation of the form $\boldsymbol{x}_P(s,n) = (s,n,m(s,n))$, with $\partial_s \boldsymbol{x}_P = \begin{bmatrix} 1 & 0 & \partial_s m \end{bmatrix}$ and $\partial_n \boldsymbol{x}_P = \begin{bmatrix} 0 & 1 & \partial_n m \end{bmatrix}$; $\partial_s(\cdot)$ and $\partial_n(\cdot)$ represent partial derivatives (with respect to s and n, respectively). Thus $\partial_s \boldsymbol{x}_P \times \partial_n \boldsymbol{x}_P = \begin{bmatrix} -\partial_s m & -\partial_n m & 1 \end{bmatrix} \neq 0$; a *Monge* parametrisation of this type is always *regular* [24,25], and can be used to model any 'fold free' surface (i.e. when $m(s,n)$ is not multi-valued).

3. 2D road models

In the planar case the road centre line can be represented parametrically by

$$\mathcal{C} = \left\{ \boldsymbol{x}_c(s) = \begin{bmatrix} x(s) & y(s) \end{bmatrix}^T \in \mathbb{R}^2 \,:\, s \in [s_0, s_f] \right\}, \tag{7}$$

in which the Cartesian coordinates are expressed in the inertial reference frame; $x(s)$ and $y(s)$ are functions of the *arc length* $s \in [s_0, s_f]$ of the curve $\mathcal{C}$. Since a road has finite width,

we introduce a lateral-displacement variable n and define a general point on the track surface by

$$\mathcal{S} = \left\{ \boldsymbol{x}_P(s,n) = \int \boldsymbol{t}\,\mathrm{d}s + \boldsymbol{n}(s)n \in \mathbb{R}^2 : s \in [s_0, s_f],\ n \in \frac{1}{2}[-r_w, r_w] \right\}. \tag{8}$$

The distance travelled along the centre line is $\int \boldsymbol{t}\,\mathrm{d}s$, while the lateral position of $\boldsymbol{x}_P(s,n)$ with respect to the centre line is n (in the $\boldsymbol{n}(s)$ direction). For closed-circuit tracks $\boldsymbol{x}_P(s_0,n_0) = \boldsymbol{x}_P(s_f,n_f)$. The track half-width r_w can be variable and is thus a function of s in these cases. In the planar case the osculating plane remains horizontal throughout the vehicle's journey with $\Omega_x = \Omega_y = 0$, and $\Omega_z \neq 0$ (unless the road section is straight).

If the centre-line survey data points shown in Figure 3 are given by $(x_i, y_i); i = 1, \ldots n$ in rectangular coordinates, a track model can be constructed as the solution of an OCP [15]. To see how this can be done, observe that

$$\mathrm{d}x = \mathrm{d}s\cos\theta \quad \mathrm{d}y = \mathrm{d}s\sin\theta, \tag{9}$$

and so

$$\frac{\mathrm{d}x}{\mathrm{d}y} = \tan\theta,$$

with the *geodesic curvature* given by

$$\Omega_z = \frac{\mathrm{d}\theta}{\mathrm{d}s} = \frac{\mathrm{d}}{\mathrm{d}s}\left(\arctan\frac{\mathrm{d}y}{\mathrm{d}x}\right). \tag{10}$$

Now let[1]

$$\Omega_z' = u; \quad \theta' = \Omega_z; \quad x' = \cos\theta; \quad y' = \sin\theta, \tag{11}$$

describe the track centre line model; u is the control input and Ω_z, θ, x and y are the state variables. The performance index to be minimised is given by

$$J = \oint_{\mathcal{C}} \left(ru^2 + (x_i - x)^2 + (y_i - y)^2\right)\mathrm{d}s, \tag{12}$$

in which x_i and y_i are interpolated values of the survey data for the track centre line. This performance index minimises the error between the measured and estimated centre-line data sets. In the case of an adaptive mesh refinement process the survey data may need to be re-sampled. The weighting r determines the importance of the rate of change of track curvature relative to the reconstruction accuracy. The weighting r can be used to low-pass filter the estimate of $\mathcal{C}$. Increasing r will 'smooth out' the states at the expense of increasing the centre-line estimation error. The introduction of the ru^2 term also serves to regularise the OCP thereby avoiding potential difficulties with singular arcs. To ensure centre-line closure, the boundary conditions $\oint_{\mathcal{C}} \Omega_z\,\mathrm{d}s = 2n\pi$ (n is an integer), $\Omega(s_0) = \Omega(s_f)$, $\theta(s_0) = \theta(s_f)$, $x(s_0) = x(s_f)$ and $y(s_0) = y(s_f)$ must be imposed. If the track has finite width, with survey data provided for the inside and outside track boundaries, a straightforward generalisation of this OCP can be used to determine the track's width and centre line as functions of s; this is a special case of the 3D OCP taught in [16].

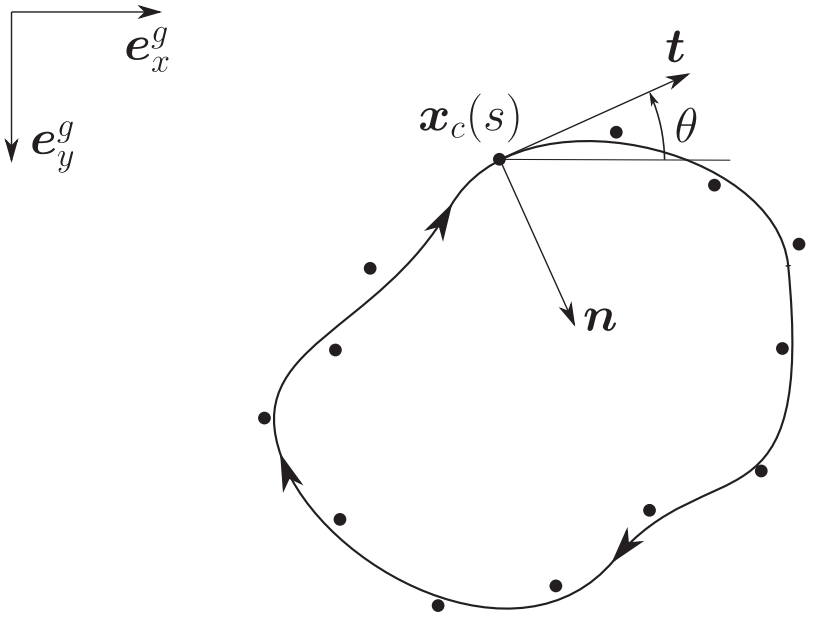


Figure 3. 2D track centre line and survey data points (x_i, y_i); $\boldsymbol{t}$, $\boldsymbol{n}$ and θ are functions of s, and $\boldsymbol{m}$ points into the page.

3.1. Velocity constraints

Contact with the road removes three of the vehicle's original six degrees of freedom. In the case of cars with a stiff suspension, the vehicle's roll and pitch freedoms are constrained by the road, while the yaw freedom is determined by driver steering. The car's longitudinal and lateral behaviour is determined by the driver, while road contact constrains the vehicle's vertical motion. We will now examine these ideas using Figure 4. Since the vehicle is travelling on a flat track, it is clear that the car's body-fixed roll and pitch angular velocities are $\omega_x^b = \omega_y^b = 0$. In order to determine its yaw angular velocity we differentiate $\psi = \theta + \chi$ with respect to time to obtain

$$\omega_z^b = \Omega_z \dot{s} + \dot{\chi} \tag{13}$$

using (10). To conclude the 2D analysis, we establish the connection between $\dot{s}$, $\dot{n}$ and the car's velocity. Using (3) we have

$$\begin{bmatrix} \dot{s} \\ \dot{n} \\ 0 \end{bmatrix} = \dot{s} \begin{bmatrix} 0 \\ n \\ 0 \end{bmatrix} \times \begin{bmatrix} 0 \\ 0 \\ \Omega_z \end{bmatrix} + \begin{bmatrix} \cos\chi & -\sin\chi & 0 \\ \sin\chi & \cos\chi & 0 \\ 0 & 0 & 1 \end{bmatrix} \begin{bmatrix} u \\ v \\ w \end{bmatrix}. \tag{14}$$

Even in the 3D case, we only need two variables on the left-hand side, because the car is travelling on a surface rather than through unrestricted space. Solving for each component, we obtain

$$\begin{bmatrix} \dot{s} \\ \dot{n} \end{bmatrix} = \begin{bmatrix} \dfrac{\cos\chi}{1 - n\Omega_z} & \dfrac{-\sin\chi}{1 - n\Omega_z} \\ \sin\chi & \cos\chi \end{bmatrix} \begin{bmatrix} u \\ v \end{bmatrix}, \tag{15}$$

with $w = 0$.

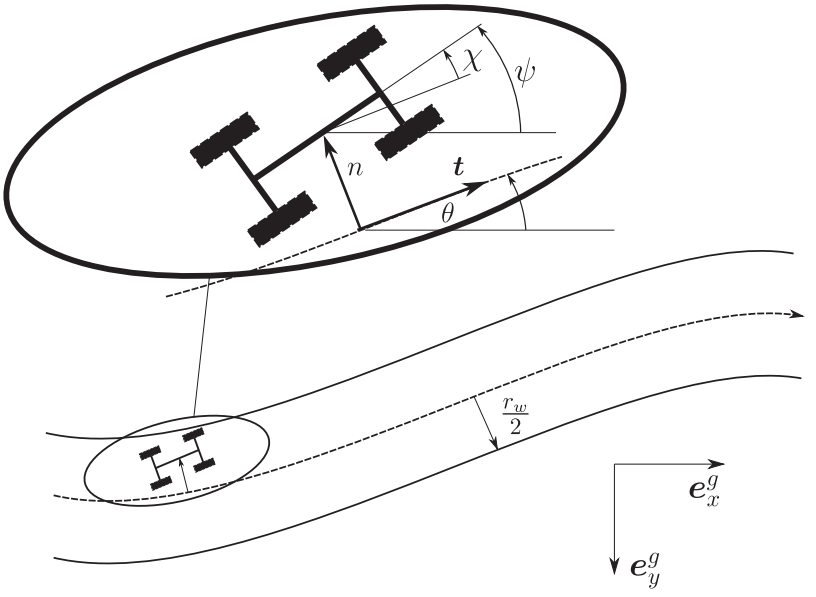


Figure 4. Vehicle on the road; $\boldsymbol{e}_x^g$ and $\boldsymbol{e}_y^g$ are basis vectors for the inertial reference frame.

4. 3D road models

Suppose that a general point on the road surface, expressed in inertial coordinates, is

$$\boldsymbol{x}_P(s,n) = x(s,n)\boldsymbol{e}_x^g + y(s,n)\boldsymbol{e}_y^g + z(s,n)\boldsymbol{e}_z^g, \tag{16}$$

where the parametric variables are again the distance travelled along the centre line and the distance from the track's centre line. An alternative parametrisation is given by

$$\mathcal{S} = \left\{ \boldsymbol{x}_P(s,n) = \int \boldsymbol{t}\,\mathrm{d}s + \boldsymbol{n}(s)n \in \mathbb{R}^3 : s \in [s_0, s_f],\ n \in \frac{1}{2}[-r_w, r_w] \right\}. \tag{17}$$

In contrast with (8), the surface is now three-dimensional.

In the 3D road model introduced in [16], the car is again assumed to travel on the osculating plane of the Darboux frame, but the osculating plane is now free to pitch and roll. Under these assumptions, the car's body-fixed angular velocity components will depend on those of the Darboux frame together with the car's yaw angle χ as defined in Figure 4. If the Darboux frame has angular velocity $\begin{bmatrix} \Omega_x & \Omega_y & \Omega_z \end{bmatrix}$, the car's body-fixed angular velocity is given by

$$\begin{bmatrix} \omega_x^b \\ \omega_y^b \\ \omega_z^b \end{bmatrix} = \dot{s} \begin{bmatrix} \cos\chi & \sin\chi & 0 \\ -\sin\chi & \cos\chi & 0 \\ 0 & 0 & 1 \end{bmatrix} \begin{bmatrix} \Omega_x \\ \Omega_y \\ \Omega_z \end{bmatrix} + \begin{bmatrix} 0 \\ 0 \\ \dot{\chi} \end{bmatrix} \tag{18}$$

as a result of the car's rotational motion by χ around $\boldsymbol{e}_z^b$; see equation (7.106) in [1]. Since the car is assumed to be travelling on the osculating plane of the Darboux frame, we need

to relate the car's velocity in body-fixed co-ordinates to its velocity expressed in Darboux co-ordinates. Using (3) there holds

$$\begin{bmatrix} \dot{s} \\ \dot{n} \\ 0 \end{bmatrix} = \begin{bmatrix} 0 \\ n \\ 0 \end{bmatrix} \times \begin{bmatrix} \omega_x^b \\ \omega_y^b \\ \omega_z^b \end{bmatrix} + \begin{bmatrix} \cos\chi & -\sin\chi & 0 \\ \sin\chi & \cos\chi & 0 \\ 0 & 0 & 1 \end{bmatrix} \begin{bmatrix} u \\ v \\ w \end{bmatrix}; \tag{19}$$

see (7.99) in [1]; these can be re-arranged to give

$$\begin{bmatrix} \dot{s} \\ \dot{n} \end{bmatrix} = \begin{bmatrix} \dfrac{\cos\chi}{1-n\Omega_z} & \dfrac{-\sin\chi}{1-n\Omega_z} \\ \sin\chi & \cos\chi \end{bmatrix} \begin{bmatrix} u \\ v \end{bmatrix} \tag{20}$$

and

$$w = \dot{s}n\Omega_x. \tag{21}$$

The car has no absolute velocity component in the Darboux frame's $\boldsymbol{m}$ direction (the car cannot leave the track surface); to ensure this (21) must hold. The next task is to find $\begin{bmatrix} \Omega_x & \Omega_y & \Omega_z \end{bmatrix}$ from track survey data.

In accordance with classical Frenet–Serret theory, the track centre line is a space curve that can be described by its curvature κ and the torsion τ. Both variables are a function of the elapsed distance s. When the centre line is 'broadened out' into a ribbon-based track description (think of a strip of tagliatelle bent to represent the road), the road's twist rate ν' is required to represent the track's camber [1]. An orthogonal basis for the Darboux frame can be described using the conventional attitude-pitch-roll convention as follows

$$R = R_z(\theta)R_y(\mu)R_x(\phi) = \begin{bmatrix} c_\theta c_\mu & c_\theta s_\mu s_\phi - s_\theta c_\phi & c_\theta s_\mu c_\phi + s_\theta s_\phi \\ s_\theta c_\mu & s_\theta s_\mu s_\phi + c_\theta c_\phi & s_\theta s_\mu c_\phi - c_\theta s_\phi \\ -s_\mu & c_\mu s_\phi & c_\mu c_\phi \end{bmatrix}, \tag{22}$$

where $R_z(\theta), R_y(\mu)$ and $R_x(\phi)$ are, respectively, elementary rotation matrices around the z, y and x axes; the columns of R represent $\begin{bmatrix} \boldsymbol{t} & \boldsymbol{n} & \boldsymbol{m} \end{bmatrix}$. The angles θ, μ and ϕ represent the attitude, slope and camber angles of the road; 's' and 'c' refer to the sine and cosine of the corresponding (subscripted) Euler angles. The *relative torsion* Ω_x, the *normal curvature* Ω_y, and the *geodesic curvature* Ω_z can be found by integrating the Euler angles [1,16]. The angular velocity of the Darboux frame is related to the Euler angles and their angular rate by

$$\begin{bmatrix} \Omega_x \\ \Omega_y \\ \Omega_z \end{bmatrix} = \begin{bmatrix} 1 & 0 & -s_\mu \\ 0 & c_\phi & c_\mu s_\phi \\ 0 & -s_\phi & c_\mu c_\phi \end{bmatrix} \begin{bmatrix} \phi' \\ \mu' \\ \theta' \end{bmatrix}, \tag{23}$$

where Ω is expressed in the body-fixed coordinates – a skew-symmetric representation of the angular rate (expressed in rad/m) is given by $R^T R'$. The location of the origin of the Darboux frame is given by

$$\begin{bmatrix} x_C \\ y_C \\ z_C \end{bmatrix} = \int \boldsymbol{t}\, \mathrm{d}s = \int \begin{bmatrix} c_\phi c_\mu \\ s_\phi c_\mu \\ -s_\mu \end{bmatrix} \mathrm{d}s. \tag{24}$$

While oriented at a general incline, this road model is assumed laterally flat, i.e. the road camber and pitch do not vary with lateral position.

5. Local curvature changes

In order to accommodate local curvature variations, it is assumed that the real road surface can vary relative to the osculating plane of the Darboux frame on the centreline [19]. In this extension the road surface is described by

$$\mathcal{S} = \left\{ \boldsymbol{x}_P(s,n) = \int \boldsymbol{t}\,\mathrm{d}s + \boldsymbol{n}(s)n + \boldsymbol{m}(s)m(s,n) \in \mathbb{R}^3 : s \in [s_0, s_f],\ n \in \frac{1}{2}[-r_w, r_w] \right\}. \tag{25}$$

The $\boldsymbol{m}(s)m(s,n)$ term introduces lateral curvature variations; see Figure 5(a). The origin of the vehicle-fixed axis system is given in terms of the vector $\boldsymbol{x}_P$ – this point is assumed to lie on the road surface and is often the projection on to the road of the vehicle's centre of mass for cars, and the rear-wheel ground contact point for motorcycles; see Figure 5(b). It is again assumed that n, and the road width r_w, are functions of s, with the position-dependent elevation $m(n,s)$ a function of both n and s. Let us assume

$$m(s,n) = \sum_{j=2}^{J} a_j(s) n^j; \tag{26}$$

one could use other functions, but algebraic functions are particularly easy to deal with mathematically. Setting $a_0(s) = a_1(s) = 0$ forces the road surface and its first-order partial derivatives to coincide with the osculating plane of the Darboux frame on the centre line. If the osculating frame is to remain tangent to the road at positions away from the centre line, the camber angle must be adjusted to $\phi(s) + \Delta\phi(s)$ and the incline changed to $\mu + \Delta\mu$, where

$$\Delta\phi(s,n) \approx \partial_n m = \sum_{j=2}^{J} j a_j(s) n^{j-1} \tag{27}$$

$$\Delta\mu(s,n) \approx -\partial_s m = -\sum_{j=2}^{J} a_j'(s) n^j; \tag{28}$$

both $\Delta\phi(s)$ and $\mu + \Delta\mu$ are assumed 'small'. The impact that these camber and inclination changes will make on the track curvature estimate at $\boldsymbol{x}_P$ can be calculated using (23) once the Euler angles have been appropriately adjusted. The transformation between absolute and road-fixed coordinates at $\boldsymbol{x}_P$ is given by the following transformation

$$R_P = R_z(\theta) R_y(\mu) R_x(\phi + \Delta\phi) R_y(\Delta\mu) = R_z(\hat{\theta}) R_y(\hat{\mu}) R_x(\hat{\phi}), \tag{29}$$

where for small angles $\Delta\phi$ and $\Delta\mu$

$$\hat{\theta} = \theta + \Delta\mu \frac{\sin\phi}{\cos\mu} \tag{30}$$

$$\hat{\mu} = \mu + \Delta\mu \cos\phi \tag{31}$$

$$\hat{\phi} = \phi + \Delta\phi + \Delta\mu \sin\phi \tan\mu. \tag{32}$$

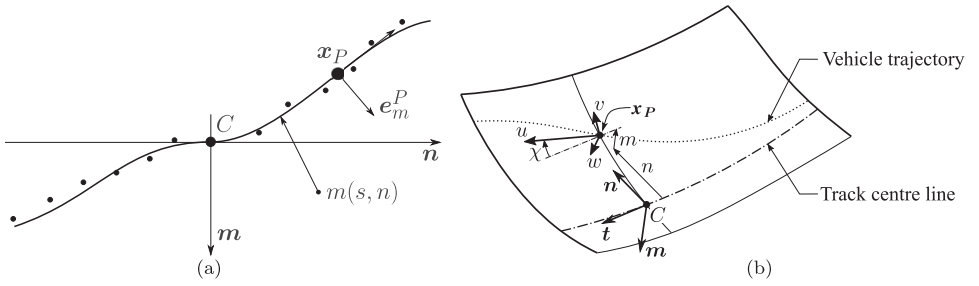


Figure 5. (a) Road cross-section represented by $m(s, n)$ with the associated LiDAR survey points; $\boldsymbol{e}_m^P$ is the road normal at $\boldsymbol{x}_P$. (b) Three-dimensional road patch and the car's position on it.

It now follows from (23) that

$$\begin{bmatrix} \hat{\Omega}_x \\ \hat{\Omega}_y \\ \hat{\Omega}_z \end{bmatrix} = \begin{bmatrix} 1 & 0 & -s_{\hat{\mu}} \\ 0 & c_{\hat{\phi}} & c_{\hat{\mu}} s_{\hat{\phi}} \\ 0 & -s_{\hat{\phi}} & c_{\hat{\mu}} c_{\hat{\phi}} \end{bmatrix} \begin{bmatrix} \hat{\phi}' \\ \hat{\mu}' \\ \hat{\theta}' \end{bmatrix}, \tag{33}$$

or what is the same

$$\begin{bmatrix} \hat{\Omega}_x \\ \hat{\Omega}_y \\ \hat{\Omega}_z \end{bmatrix} = R_y^T(\Delta\mu) R_x^T(\Delta\phi) \begin{bmatrix} \Omega_x \\ \Omega_y \\ \Omega_z \end{bmatrix} + R_y^T(\Delta\mu) \begin{bmatrix} \Delta\phi' \\ 0 \\ 0 \end{bmatrix} + \begin{bmatrix} 0 \\ \Delta\mu' \\ 0 \end{bmatrix}. \tag{34}$$

The first term on the right-hand side expresses $\boldsymbol{\Omega}$ as a rotationally adjusted Darboux frame angular velocity resulting from the introduction of $m(s, n)$, while the second and third terms recognise the additional angular road rates resulting from the partial derivatives given in (27) and (28). In this model the vehicle is re-oriented along with the Darboux frame, in accordance with the first-order partial derivatives of $m(s, n)$.

5.1. Velocity constraints

The vehicle's position on the road surface is again described in terms of s, n, and its orientation χ relative to the Darboux frame tangent vector. More particularly, χ is a rotation about the road normal $\boldsymbol{e}_m^P$ at $\boldsymbol{x}_P$, and is measured relative to $\boldsymbol{t}$; see Figure 5(b). The relationship between s, n, χ, and the absolute velocity $[u, v, w]^T$ of the reference point $\boldsymbol{x}_P$ (expressed in the vehicle's body-fixed reference frame) can now be found using (3). That is

$$\begin{aligned} \begin{bmatrix} \dot{s} \\ \dot{n} \\ \dot{m} \end{bmatrix} &= \begin{bmatrix} 0 \\ n \\ m \end{bmatrix} \times \dot{s}\boldsymbol{\Omega}^0 + R_x(\Delta\phi) R_y(\Delta\mu) R_z(\chi) \begin{bmatrix} u \\ v \\ w \end{bmatrix} \\ &\approx \begin{bmatrix} uc_\chi - vs_\chi + w\Delta\mu \\ us_\chi + vc_\chi - w\Delta\phi \\ w + \Delta\phi(us_\chi + vc_\chi) - \Delta\mu(uc_\chi - vs_\chi) \end{bmatrix}, \end{aligned} \tag{35}$$

where $\Delta\phi$ and $\Delta\mu$ are treated as 'small'; see equations (7.99) and (7.100) in [1]. The temporal elevation rate due to $m(s,n)$ is given by

$$\dot{m} = \dot{n}\partial_n m + \dot{s}\partial_s m \tag{36}$$

$$= \sum_{j=2}^{J} \left(\dot{n} j a_j n^{j-1} + \dot{s} a_j' n^j \right). \tag{37}$$

Equation (35) can be solved to give

$$\dot{s} = \frac{u c_\chi - v s_\chi}{1 - n\Omega_z + m\Omega_y + n\Omega_x \partial_s m} \tag{38}$$

$$\dot{n} = u \sin\chi + v\cos\chi + (m - n\partial_n m)\,\Omega_x \dot{s}, \tag{39}$$

$$w = n\,(\Omega_x + \Omega_z \partial_s m)\,\dot{s}. \tag{40}$$

The temporal angular velocity $[\omega_x^b, \omega_y^b, \omega_z^b]^T$ of the vehicle in body-fixed coordinates, and the road curvature at point $\boldsymbol{x}_P$ are related by

$$\begin{bmatrix} \omega_x^b \\ \omega_y^b \\ \omega_z^b \end{bmatrix} = R_z^T(\chi) \begin{bmatrix} \hat{\Omega}_x \\ \hat{\Omega}_y \\ \hat{\Omega}_z \end{bmatrix} \dot{s} + \begin{bmatrix} 0 \\ 0 \\ \dot{\chi} \end{bmatrix}$$

$$= \begin{bmatrix} (\hat{\Omega}_x c_\chi + \hat{\Omega}_y s_\chi)\dot{s} \\ (\hat{\Omega}_y c_\chi - \hat{\Omega}_x s_\chi)\dot{s} \\ \hat{\Omega}_z \dot{s} + \dot{\chi} \end{bmatrix} \tag{41}$$

where $[\hat{\Omega}_x, \hat{\Omega}_y, \hat{\Omega}_z]^T$ is given by (34). These equations are identical to those given in (13) and (18) once the road curvatures of the centre line are replaced by those at $\boldsymbol{x}_P$.

6. Road reconstruction

The OCP associated with road reconstruction is again of the general form

$$\underset{\boldsymbol{u}}{\text{minimise}} \quad J = \oint_{\mathcal{C}} (S(\boldsymbol{x}) + U(\boldsymbol{x}))\,\mathrm{d}s, \tag{42}$$

$$\text{subject to} \quad \frac{\mathrm{d}\boldsymbol{x}}{\mathrm{d}s} = \boldsymbol{f}(\boldsymbol{x}, \boldsymbol{u}), \tag{43}$$

where the displacement is along the centre line and around the closed centre line $\mathcal{C}$. The performance index J is chosen to minimise errors relative to the survey data, while the function $\boldsymbol{f}(\boldsymbol{x}, \boldsymbol{u})$ encapsulates the track's geometric constraints. It is important that the track model is sufficiently smooth, because it is passed subsequently to a minimum-time OCP and a noise track model may cause numerical issues there. See [1,16,19] for further details.

The model state vector comprises three position variables, integrator chains for each of the Euler angles, a road-width variable, and states relating to the polynomial coefficients

in (26) and their derivatives. Depending on the application, the integrator chains may vary in length. The state variables may be assembled as

$$\boldsymbol{x} = [x_C, y_C, z_C, \phi, \phi', \phi'', \mu, \mu', \mu'', \theta, \theta', \theta'', r_w, a_2, \ldots, a_J, a_2', \ldots, a_J', a_2'', \ldots, a_J'']^T. \quad (44)$$

The model controls manipulate the trajectory of the Darboux frame so that it circumnavigates the race track, while minimising an estimation error. These inputs relate to the Euler angles, the road width, and the polynomial coefficients, and are given by

$$\boldsymbol{u} = [u_\phi, u_\mu, u_\theta, u_{rw}, u_{a2}, \ldots, u_{aJ}]^T. \quad (45)$$

The system equations are

$$\begin{aligned}\boldsymbol{f}(\boldsymbol{x}, \boldsymbol{u}) = [&c_\theta c_\mu, s_\theta c_\mu, -s_\mu, \phi', \phi'', u_\phi, \mu', \mu'', u_\mu, \theta', \theta'', u_\theta, u_{rw},\\ &a_2', \ldots, a_J', a_2'', \ldots, a_J'', u_{a2}, \ldots, u_{aJ}]^T; \end{aligned} \quad (46)$$

the first column of (22) gives the tangent direction. The state- and control-related terms in the performance index (42) are

$$U(\boldsymbol{u}) = W_\phi u_\phi^2 + W_\mu u_\mu^2 + W_\theta u_\theta^2 + W_{rw} u_{rw}^2 + \sum_{j=2}^{J} W_{aj} u_{aj}^2, \quad (47)$$

$$S(\boldsymbol{x}) = \sum_{k=1}^{K} \left(Q_x (x_k - x_{k0})^2 + Q_y (y_k - y_{k0})^2 + Q_z (z_k - z_{k0})^2 \right). \quad (48)$$

The quantities

$$x_k = x_C + (c_\theta s_\mu s_\phi - s_\theta c_\phi) n_k + (s_\theta s_\phi + c_\theta s_\mu c_\phi) m_k, \quad (49)$$

$$y_k = y_C + (c_\theta c_\phi + s_\theta s_\mu s_\phi) n_k + (s_\theta s_\mu c_\phi - c_\theta s_\phi) m_k, \quad (50)$$

$$z_k = z_C + c_\mu s_\phi n_k + c_\mu c_\phi m_k, \quad (51)$$

are position estimates relating to track centre line and the survey stations either side of it. The control weights are W_ϕ, W_μ, W_θ, W_{rw}, and W_{aj}, while Q_x, Q_y, and Q_x are weights on the track-model estimation errors. Since the survey data is assumed equispaced, n_k is given by

$$n_k = -\frac{r_w}{2} + \frac{k-1}{K-1} r_w, \quad k = 1, \ldots, K \quad (52)$$

where r_w is the track-width estimate. Equispaced data can always be obtained from non-uniformly-spaced data by interpolation and re-sampling so that $\Delta n_k / r_w$ is constant. The height estimates come from (26) and are given by $m_k = m(n_k, s)$ for each k and all s. The optimal estimation problem is to minimise the error from the track survey data given by x_{k0}, y_{k0}, and z_{k0}; see Figure 5(a).

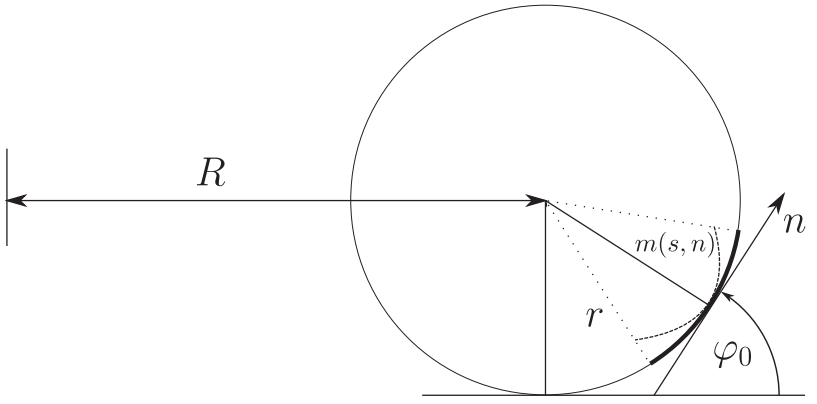


Figure 6. Race track on the interior surface of a toroidal shell – shown as a heavy black curve. The major toroidal radius is R, the minor radius is r, with the track surface defined by $\varphi \in [\varphi_{min}, \varphi_{max}]$.

In the case of closed race tracks, cyclic boundary conditions must be enforced. These are

$$\boldsymbol{x}(s_i) = \boldsymbol{x}(s_f) \tag{53}$$

for all the state variable except the yaw angle θ. In this case

$$\theta(s_i) - \theta(s_f) = \pm 2\pi, \tag{54}$$

with the sign determined by the track running direction.

Example 6.1: Some of the key track-modelling concepts will now be illustrated with an idealised 'track' that has the toroidal geometry illustrated in Figure 6.

In rectangular coordinates a toroidal shell can be described by

$$x = (R + r\sin\varphi)\cos\theta \tag{55}$$

$$y = (R + r\sin\varphi)\sin\theta \tag{56}$$

$$z = r(1 - \cos\varphi) \tag{57}$$

with $\theta \in [0, 2\pi]$. By expanding (57) as a Taylor series around φ_0 to third order, we obtain

$$z \approx r(1 - \cos\varphi_0) + r\Delta\varphi\sin\varphi_0 + \frac{r}{2}(\Delta\varphi)^2\cos\varphi_0 - \frac{r}{6}(\Delta\varphi)^3\sin\varphi_0 + \mathcal{O}\left((\Delta\varphi)^4\right). \tag{58}$$

The first two terms define a plane tangent to the toroidal surface at φ_0; the osculating plane of the Darboux frame. The third and fourth terms describe the way in which the road surface 'bends away' from the tangent plane.

The distance between the tangent plane and the toroidal surface is given by

$$\bar{z} = \sqrt{r^2 - n^2} - r \Rightarrow m(s,n) = -\frac{n^2}{2r} - \frac{n^4}{8r^3} + \mathcal{O}(n^5); \tag{59}$$

the s variable does not appear due to the cylindrical symmetry of this idealised track.

Table 1. Optimised track model parameters.

$\dot{\theta} = -1.9429 \times 10^{-3}\, r/m$	$\mu = 0$	$\phi = 25^o$
$\Omega_x = 0.0$	$\Omega_y = 8.0652 \times 10^{-4}\, r/m$	$\Omega_z = -1.7677 \times 10^{-3}\, r/m$
$a_2 = -1.4897 \times 10^{-2}$	$a_3 = -4.0747 \times 10^{-4}$	–

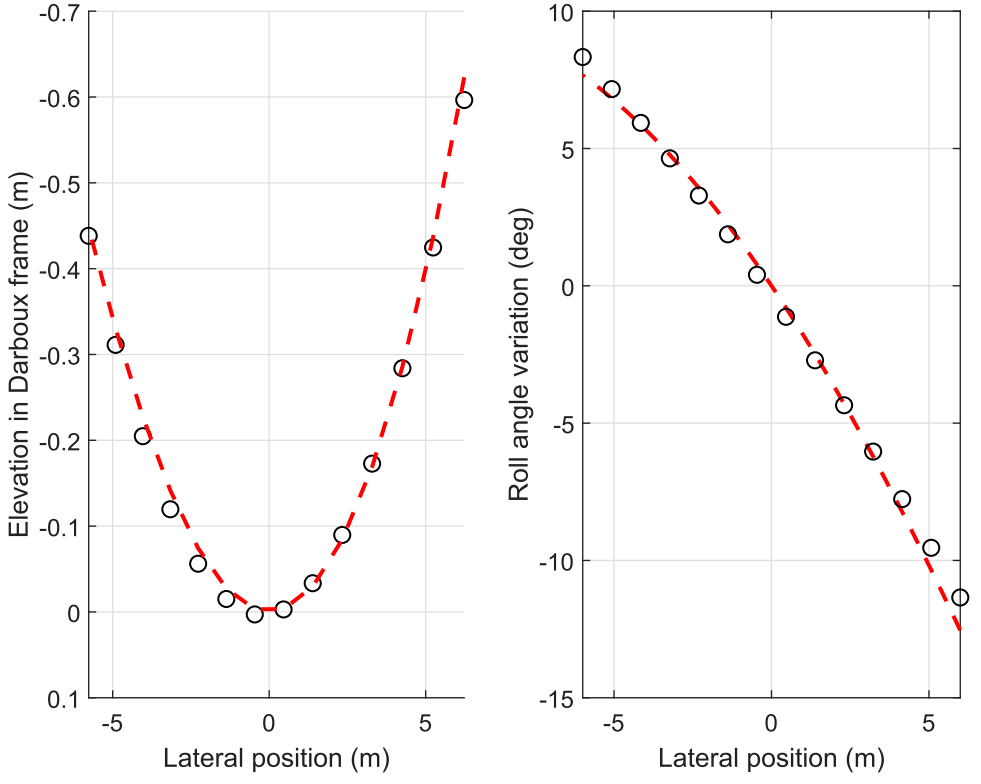


Figure 7. Model predictions (red dashed) and 'raw toroidal data' (black circles). The left-hand figure shows the height prediction $m(s, n)$, while the right-hand figure shows the camber-angle variation prediction using (27).

For the case $R = 500$ m, $r = 35$ m, $r_w = 12$ m and $\varphi_0 = 25$ deg, the optimal track-modelling parameters are given in Table 1 for $J = 3$ in (26).

Figure 7 shows the optimised track model for the track surface height variation above the osculating plane of the Darboux frame, and the variation of camber angle with track lateral position. Note that the truncated Taylor series expansion with $a_2 = -\frac{1}{2r}$ and $a_3 = 0$ does not constitute an optimal set of polynomial coefficients!

7. Alternative approach

Returning to the road parametrisation given in (25), we note that this is a parametrisation of *Monge* type [23]. Next, we introduce a fourth coordinate system that rotates relative to $\boldsymbol{e}_z^b$ and is used to describe the local road surface under the car [18]. Following standard differential-geometric arguments, we define vectors $\partial_s \boldsymbol{x}_P$ and $\partial_n \boldsymbol{x}_P$, which span the

plane tangent to the road surface at $\boldsymbol{x}_P$. Due to the regularity of the road surface these partial derivatives are both non-zero and independent. These vectors together with the local surface normal

$$\boldsymbol{e}_m^P = \frac{\partial_s \boldsymbol{x}_P \times \partial_n \boldsymbol{x}_P}{\|\partial_s \boldsymbol{x}_P \times \partial_n \boldsymbol{x}_P\|} \tag{60}$$

define another trihedron (that is not generally orthonormal).

The car's heading angle χ is now the angle between $\boldsymbol{e}_x^b$ and $\partial_s \boldsymbol{x}_P$ – this is not the same as the heading angle defined in prior literature, which is the angle between $\boldsymbol{e}_x^b$ and $\boldsymbol{t}$ [16,26]. Since the road-surface normal at $\boldsymbol{x}_P$ is parallel to the body-fixed z-axis, there holds

$$\boldsymbol{e}_z^b = \boldsymbol{e}_m^P. \tag{61}$$

It follows from (60) and (61) that

$$\boldsymbol{e}_z^b.\partial_s \boldsymbol{x}_P = 0 \tag{62}$$

$$\boldsymbol{e}_z^b.\partial_n \boldsymbol{x}_P = 0. \tag{63}$$

These constraint equations again restrict the car to a single rotational freedom (around the surface normal), which we will now examine.

A plan view of the contact point $\boldsymbol{x}_P$ and its surrounding contact patch is given in Figure 8. From this figure one can immediately deduce that

$$\cos\chi = \frac{\boldsymbol{e}_x^b.\partial_s \boldsymbol{x}_P}{\|\partial_s \boldsymbol{x}_P\|} \quad \text{and} \quad \sin\chi = -\frac{\boldsymbol{e}_y^b.\partial_s \boldsymbol{x}_P}{\|\partial_s \boldsymbol{x}_P\|} \tag{64}$$

and

$$\cos\xi = \frac{\boldsymbol{e}_y^b.\partial_n \boldsymbol{x}_P}{\|\partial_n \boldsymbol{x}_P\|} \quad \text{and} \quad \sin\xi = \frac{\boldsymbol{e}_x^b.\partial_n \boldsymbol{x}_P}{\|\partial_n \boldsymbol{x}_P\|}; \tag{65}$$

it is evident that

$$\xi = \frac{\pi}{2} - \arccos\left(\frac{\partial_s \boldsymbol{x}_P.\partial_n \boldsymbol{x}_P}{\|\partial_s \boldsymbol{x}_P\|.\|\partial_n \boldsymbol{x}_P\|}\right) + \chi. \tag{66}$$

When $\partial_s \boldsymbol{x}_P$ and $\partial_n \boldsymbol{x}_P$ are orthogonal $\xi = \chi$. It is shown in [18] that

$$\dot{\chi} = \omega_z^b + \frac{(\partial_{ss}\boldsymbol{x}_P \times \partial_s \boldsymbol{x}_P).\boldsymbol{e}_m^p}{\partial_s \boldsymbol{x}_P.\partial_s \boldsymbol{x}_P}\dot{s} + \frac{(\partial_{sn}\boldsymbol{x}_P \times \partial_s \boldsymbol{x}_P).\boldsymbol{e}_m^p}{\partial_s \boldsymbol{x}_P.\partial_s \boldsymbol{x}_P}\dot{n}. \tag{67}$$

A similar calculation shows that

$$\dot{\xi} = \omega_z^b + \frac{(\partial_{sn}\boldsymbol{x}_P \times \partial_n \boldsymbol{x}_P).\boldsymbol{e}_m^p}{\partial_n \boldsymbol{x}_P.\partial_n \boldsymbol{x}_P}\dot{s} + \frac{(\partial_{nn}\boldsymbol{x}_P \times \partial_n \boldsymbol{x}_P).\boldsymbol{e}_m^p}{\partial_n \boldsymbol{x}_P.\partial_n \boldsymbol{x}_P}\dot{n}. \tag{68}$$

In view of (66), one of (67) and (68) is mathematically redundant, but both are retained for approximation and computational purposes.

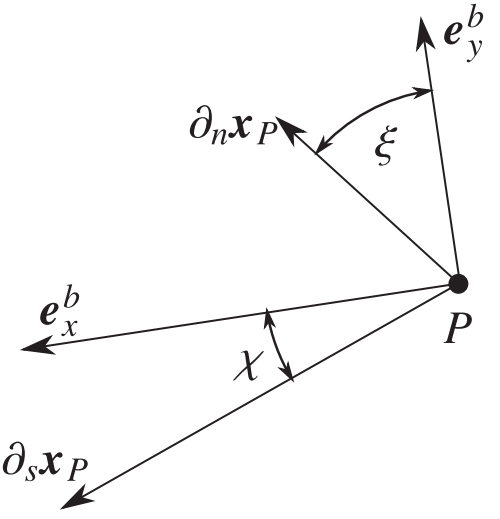


Figure 8. Heading angle χ and heading co-angle ξ.

7.1. Translational velocity constraint

Our purpose here is to relate the parametric and body-fixed linear velocities. The velocity of $\boldsymbol{x}_P$ is given by

$$\frac{\mathrm{d}}{\mathrm{d}t}\boldsymbol{x}_P = \partial_s \boldsymbol{x}_P \dot{s} + \partial_n \boldsymbol{x}_P \dot{n}, \tag{69}$$

which means that

$$\partial_s \boldsymbol{x}_P \dot{s} + \partial_n \boldsymbol{x}_P \dot{n} = u\boldsymbol{e}_x^b + v\boldsymbol{e}_y^b + w\boldsymbol{e}_z^b, \tag{70}$$

where u, v and w are the body-fixed components of the car's linear velocity. Dotting this equation with $\boldsymbol{e}_z^b$ shows that

$$w = 0, \tag{71}$$

since each of the remaining vectors are in the plane tangent to the road surface. We can now dot (70) with $\partial_s \boldsymbol{x}_P$ and $\partial_n \boldsymbol{x}_P$, while recognising (71), to obtain

$$\begin{bmatrix} \partial_s \boldsymbol{x}_P.\partial_s \boldsymbol{x}_P & \partial_s \boldsymbol{x}_P.\partial_n \boldsymbol{x}_P \\ \partial_n \boldsymbol{x}_P.\partial_s \boldsymbol{x}_P & \partial_n \boldsymbol{x}_P.\partial_n \boldsymbol{x}_P \end{bmatrix} \begin{bmatrix} \dot{s} \\ \dot{n} \end{bmatrix} = \begin{bmatrix} \partial_s \boldsymbol{x}_P.\boldsymbol{e}_x^b & \partial_s \boldsymbol{x}_P.\boldsymbol{e}_y^b \\ \partial_n \boldsymbol{x}_P.\boldsymbol{e}_x^b & \partial_n \boldsymbol{x}_P.\boldsymbol{e}_y^b \end{bmatrix} \begin{bmatrix} u \\ v \end{bmatrix}. \tag{72}$$

In conformity with standard differential-geometric notation,

$$I = \begin{bmatrix} \partial_s \boldsymbol{x}_P.\partial_s \boldsymbol{x}_P & \partial_s \boldsymbol{x}_P.\partial_n \boldsymbol{x}_P \\ \partial_n \boldsymbol{x}_P.\partial_s \boldsymbol{x}_P & \partial_n \boldsymbol{x}_P.\partial_n \boldsymbol{x}_P \end{bmatrix} \tag{73}$$

is called the *first fundamental form*, which facilitates the calculation of metric properties such as 'length' [2]. It follows from (64) and (65) that

$$J = \begin{bmatrix} \partial_s \boldsymbol{x}_P.\boldsymbol{e}_x^b & \partial_s \boldsymbol{x}_P.\boldsymbol{e}_y^b \\ \partial_n \boldsymbol{x}_P.\boldsymbol{e}_x^b & \partial_n \boldsymbol{x}_P.\boldsymbol{e}_y^b \end{bmatrix} = \begin{bmatrix} \cos\chi \,\|\partial_s \boldsymbol{x}_P\| & -\sin\chi \,\|\partial_s \boldsymbol{x}_P\| \\ \sin\xi \,\|\partial_n \boldsymbol{x}_P\| & \cos\xi \,\|\partial_n \boldsymbol{x}_P\| \end{bmatrix}, \tag{74}$$

and so

$$\begin{bmatrix} \dot{s} \\ \dot{n} \end{bmatrix} = I^{-1} J \begin{bmatrix} u \\ v \end{bmatrix}, \tag{75}$$

constrains the way in which $\dot{s}$ and $\dot{n}$ can evolve given u and v. The regularity of the road surface implies the invertibility of the first fundamental form [24].

7.2. Angular velocity constraint

Since the car is assumed to have no suspension, its roll and pitch motions are dictated by those of the road surface. This suggests a nonholonomic constraint that governs ω_x^b and ω_y^b in terms of u and v. Differentiating (62) and (63) with respect to time gives

$$0 = \frac{\mathrm{d}}{\mathrm{d}t}(\boldsymbol{e}_z^b).\partial_s \boldsymbol{x}_P + \boldsymbol{e}_z^b.\frac{\mathrm{d}}{\mathrm{d}t}(\partial_s \boldsymbol{x}_P) \tag{76}$$

$$0 = \frac{\mathrm{d}}{\mathrm{d}t}(\boldsymbol{e}_z^b).\partial_n \boldsymbol{x}_P + \boldsymbol{e}_z^b.\frac{\mathrm{d}}{\mathrm{d}t}(\partial_n \boldsymbol{x}_P). \tag{77}$$

Eliminating the $\frac{\mathrm{d}}{\mathrm{d}t}(\boldsymbol{e}_z^b)$ terms using (4), and expanding the time derivatives of the partial derivative terms gives

$$\left(\begin{bmatrix} \partial_s \boldsymbol{x}_P \\ \partial_n \boldsymbol{x}_P \end{bmatrix} . \begin{bmatrix} \boldsymbol{e}_x^b & \boldsymbol{e}_y^b \end{bmatrix} = J \right) \begin{bmatrix} -\omega_y^b \\ \omega_x^b \end{bmatrix} = \begin{bmatrix} \boldsymbol{e}_m^P.\partial_{ss}\boldsymbol{x}_P & \boldsymbol{e}_m^P.\partial_{sn}\boldsymbol{x}_P \\ \boldsymbol{e}_m^P.\partial_{ns}\boldsymbol{x}_P & \boldsymbol{e}_m^P.\partial_{nn}\boldsymbol{x}_P \end{bmatrix} \begin{bmatrix} \dot{s} \\ \dot{n} \end{bmatrix} \tag{78}$$

where

$$II = \begin{bmatrix} \boldsymbol{e}_m^P.\partial_{ss}\boldsymbol{x}_P & \boldsymbol{e}_m^P.\partial_{sn}\boldsymbol{x}_P \\ \boldsymbol{e}_m^P.\partial_{ns}\boldsymbol{x}_P & \boldsymbol{e}_m^P.\partial_{nn}\boldsymbol{x}_P \end{bmatrix} \tag{79}$$

is the *second fundamental form* that is used to study local surface curvature [23,24] [3]. The constraint on ω_x^b and ω_y^b is thus

$$\begin{bmatrix} -\omega_y^b \\ \omega_x^b \end{bmatrix} = J^{-1}(II)I^{-1}J \begin{bmatrix} u \\ v \end{bmatrix}. \tag{80}$$

Since $J^{-1}(\cdot)J$ is a similarity transformation on $(II)I^{-1}$, the eigenvalues of $J^{-1}(II)I^{-1}J$ are the principle curvature of the road surface at $\boldsymbol{x}_P$.

7.3. Parametrisation for the Darlington raceway

The track parametrisation given in (6) can become computationally unwieldy due the proliferation of numerous 'small' terms. These track-specific small terms may include: $\partial_{sn}m$, $\partial_{nn}m$, $\Omega_x\Omega_y m$, $\Omega_x^2 m$, $\Omega_y^2 m$, $\Omega_y\Omega_z m$, Ω_x^3, Ω_y^3, Ω_z^3, $\Omega_x^2\Omega_y$, $\Omega_y^2\Omega_z$, $(\partial_n m)^2$, and $m\partial_n m$.

Following a number of track-specific simplifications [20], using (6) and (4) one obtains

$$\partial_s \boldsymbol{x}_P = (1 + \Omega_y m - n\Omega_z)\boldsymbol{t} + \Omega_x(n\boldsymbol{m} - m\boldsymbol{n}) \tag{81}$$

$$\partial_n \boldsymbol{x}_P = \boldsymbol{n} + \boldsymbol{m}\partial_n m \tag{82}$$

$$\begin{aligned}\partial_{ss} \boldsymbol{x}_P = {} & (m\partial_s\Omega_y - n\partial_s\Omega_z + \Omega_x(n\Omega_y + m\Omega_z))\boldsymbol{t} \\ & + (\Omega_z - m\partial_s\Omega_x - n(\Omega_x^2 + \Omega_z^2))\boldsymbol{n} \\ & + (n(\partial_s\Omega_x + \Omega_y\Omega_z) - \Omega_y)\boldsymbol{m}\end{aligned} \tag{83}$$

$$\partial_{sn} \boldsymbol{x}_P = (\Omega_y\partial_n m - \Omega_z)\boldsymbol{t} + (-\Omega_x\partial_n m)\boldsymbol{n} + \Omega_x\boldsymbol{m} \tag{84}$$

$$\partial_{nn} \boldsymbol{x}_P = 0. \tag{85}$$

Clearly $\partial_s \boldsymbol{x}_P$ and $\partial_n \boldsymbol{x}_P$ are predominantly in the $\boldsymbol{t}$ and $\boldsymbol{n}$ directions, respectively.

The car's heading co-angle comes from (68) and is given by

$$\dot{\xi} = \omega_z^b + \dot{s}\left(\frac{n(\Omega_x^2 + \Omega_z^2) - \Omega_z + \Omega_y\partial_n m(1 - n\Omega_z)}{\sqrt{n^2\Omega_x^2 + (1 - n\Omega_z)^2 + 2m\Omega_y}}\right). \tag{86}$$

This differential equation is used, because it is less cumbersome to work with than its counterpart (67). The heading and co-heading angles χ and ξ are related by

$$\chi = \arccos\left(\frac{\Omega_x(n\partial_n m - m)}{\sqrt{n^2\Omega_x^2 + (1 - n\Omega_z)^2 + 2m\Omega_y}}\right) - \frac{\pi}{2} + \xi; \tag{87}$$

$\chi \approx \xi$ when $n\partial_n m - m$ is 'small'. The first fundamental form comes from (73) and is given by

$$I = \begin{bmatrix} n^2\Omega_x^2 + (1 - n\Omega_z)^2 + 2m\Omega_y & \Omega_x(n\partial_n m - m) \\ \Omega_x(n\partial_n m - m) & 1 \end{bmatrix}. \tag{88}$$

The Jacobian (74) is given by

$$J = \begin{bmatrix} \cos\chi\sqrt{n^2\Omega_x^2 + (1 - n\Omega_z)^2 + 2m\Omega_y} & -\sin\chi\sqrt{n^2\Omega_x^2 + (1 - n\Omega_z)^2 + 2m\Omega_y} \\ \sin\xi & \cos\xi \end{bmatrix}, \tag{89}$$

which allows (75) to be evaluated.

The second fundamental form (79) is given by

$$II = \frac{1}{a}\begin{bmatrix} n\partial_s\Omega_x + n^2(\Omega_x\partial_s\Omega_z - \Omega_z\partial_s\Omega_x) + nm(\Omega_y\partial_s\Omega_x - \Omega_x\partial_s\Omega_y) & f \\ -\Omega_y(1 - n\Omega_z)^2 & 0 \\ f & \end{bmatrix}, \tag{90}$$

where

$$a = \sqrt{n^2\Omega_x^2 + (1 - n\Omega_z)^2 + 2m\Omega_y} \quad \text{and} \quad f = \Omega_x(1 - n\Omega_y\partial_n m) \approx \Omega_x,$$

which allows (80) to be solved. The optimisation of the track parameters exploit the OCP described in Section 6.

8. Results and critique

We now review the similarities and differences between the recently developed models described in Section 5 (the first model) and Section 7 (the second model). We give illustrative calculations in the case that $m(s,n)=0$. We will then compare the results of minimum-lap-time computations produced by these models in the general case that $m(s,n)\neq 0$.

In both models $\dot{s}$ describes the velocity of the Darboux frame in the $\boldsymbol{t}$ direction, while n describes the lateral displacement of the car in the $\boldsymbol{n}$ direction in Darboux co-ordinates. In the first model the car travels on the osculating plane of a 'corrected' Darboux frame, while in the second model the car travels on a plane tangent to the road surface immediately under the car. In the first model the tangent plane is the span of $\boldsymbol{t}$ and $\boldsymbol{n}$, while in the second it is the span of $\partial_s \boldsymbol{x}_P$ and $\partial_n \boldsymbol{x}_P$.

When $m(s,n)=0$, the road-surface normal for the second model is given by [4]:

$$\boldsymbol{e}_m^P = \frac{\boldsymbol{m} - n(\Omega_x \boldsymbol{t} + \Omega_z \boldsymbol{m})}{\sqrt{n^2\Omega_x^2 + (1-n\Omega_z)^2}} \approx \boldsymbol{m} - \frac{n\Omega_x \boldsymbol{t}}{1-n\Omega_z} \tag{91}$$

which is predominately in the $\boldsymbol{m}$ direction, and parallel to it when $n=0$ and/or the road is torsion-free. When the track has torsion, the tangent plane under the car twists away from the Darboux frame as the car moves laterally.

The first model describes a car yawing through χ – the angle between $\boldsymbol{t}$ and $\boldsymbol{e}_x^b$; see Figure 4. The body-fixed axis $\boldsymbol{e}_z^b$ is parallel to $\boldsymbol{m}$ and offset from it by distance n; $m(s,n)$ is used to adjust the orientation of the Darboux frame using (30), (31) and (32). The car's velocity is related to the speed of the origin of the Darboux frame along the centre line and the lateral speed $\dot{n}$ by (38) and (39). The car's angular velocity (in body fixed coordinates) is given by (41). In order to keep the car on the road, the vertical component of the car's velocity is given by (21).

In the second model the car travels on the local road-surface tangent plan spanned by $\partial_s \boldsymbol{x}_P$ and $\partial_n \boldsymbol{x}_P$. The car has yaw angle χ and yaw co-angle ξ as defined in Figure 8; *the yaw angles in the two models are different, while $\partial_s \boldsymbol{x}_P$ and $\partial_n \boldsymbol{x}_P$ need not be orthogonal*. It is clear from (81) that $\partial_s \boldsymbol{x}_P$ is substantially in the $\boldsymbol{t}$ direction, with a difference coming from the torsion term. The $\partial_n \boldsymbol{x}_P$ vector is substantial in the $\boldsymbol{n}$ direction, with small differences coming from $\partial_n m$. In the second model the car's normal velocity component is zero; see (71). The car's velocity in Darboux coordinates is given by (75), while the angular velocity of the car is given by (80). When $m(s,n)=0$, (75) becomes

$$\begin{bmatrix} \dot{s} \\ \dot{n} \end{bmatrix} = \begin{bmatrix} \dfrac{\cos\chi}{\sqrt{(n\Omega_x)^2 + (1-n\Omega_z)^2}} & \dfrac{-\sin\chi}{\sqrt{(n\Omega_x)^2 + (1-n\Omega_z)^2}} \\ \sin\chi & \cos\chi \end{bmatrix} \begin{bmatrix} u \\ v \end{bmatrix} \tag{92}$$

and the $\dot{s}$ expression above differs from that in (15) by virtue of the torsional term $n\Omega_x$. If the road is not heavily 'corkscrewed', a power series expansion of the denominator term results in

$$\begin{bmatrix} \dot{s} \\ \dot{n} \end{bmatrix} \approx \begin{bmatrix} \dfrac{\cos\chi}{1-n\Omega_z} & \dfrac{-\sin\chi}{1-n\Omega_z} \\ \sin\chi & \cos\chi \end{bmatrix} \begin{bmatrix} u \\ v \end{bmatrix}, \tag{93}$$

with the $\dot{s}$ expression matching (15). The $\dot{n}$ term in equations (15), (39) and (93) are all the same. If $m(s,n)=0$, $\partial_s \boldsymbol{x}_P$ and $\partial_n \boldsymbol{x}_P$ are orthogonal with $\boldsymbol{n}$ and $\partial_n \boldsymbol{x}_P$ parallel; see (82). Equation (81) shows that the torsion term causes $\partial_s \boldsymbol{x}_P$ to rotates away from $\boldsymbol{t}$, around the $\boldsymbol{n}$-axis, as n increases. This 'twisting' away from osculating plane of the Darboux frame is evident in (91), which contains an n-related term in the $\boldsymbol{t}$ direction. Equations (41) and (80) provide the car's x- and y-axis angular velocity constraints as imposed by the curvature of the road. Equation (41) recognises the local surface curvature by adapting the orientation of the Darboux frame to the local conditions under the car. Equation (80) describes the curvature of the road under the car in terms of the principle curvatures as described in classical differential geometry and the second fundamental form[23,24].

If $m(s,n)=0$ one can obtain a simple expression for the principle curvatures of the road under the car. Setting

$$\sigma = \sqrt{n^2\Omega_x^2 + (1-n\Omega_z)^2} \approx (1-n\Omega_z),$$

it follows by direct calculation that

$$I = \begin{bmatrix} \sigma^2 & 0 \\ 0 & 1 \end{bmatrix}; \quad II \approx \frac{1}{\sigma}\begin{bmatrix} -\Omega_y & \Omega_x \\ \Omega_x & 0 \end{bmatrix} \quad \text{and} \quad (II)I^{-1} \approx \frac{1}{\sigma^3}\begin{bmatrix} -\Omega_y & \sigma^2\Omega_x \\ \Omega_x & 0 \end{bmatrix} \tag{94}$$

with the principle curvatures at $\boldsymbol{x}_P$ given by

$$\kappa_n \approx \frac{-\Omega_y \pm \sqrt{\Omega_y^2 + 4\sigma^2\Omega_x^2}}{2\sigma^3}. \tag{95}$$

The principle curvatures of the osculating plane of the Darboux frame are both zero.

When $m(s,n)=0$ (78) becomes

$$\begin{bmatrix} -\omega_y^b \\ \omega_x^b \end{bmatrix} = J^{-1}II\begin{bmatrix} \dot{s} \\ \dot{n} \end{bmatrix} \approx \begin{bmatrix} \dfrac{-\Omega_y\cos\chi}{(1-n\Omega_z)^2} + \dfrac{\Omega_x\sin\chi}{1-n\Omega_z} & \dfrac{\Omega_x\cos\chi}{(1-n\Omega_z)^2} \\ \dfrac{\Omega_y\sin\chi}{(1-n\Omega_z)^2} + \dfrac{\Omega_x\cos\chi}{1-n\Omega_z} & \dfrac{-\Omega_x\sin\chi}{(1-n\Omega_z)^2} \end{bmatrix}\begin{bmatrix} \dot{s} \\ \dot{n} \end{bmatrix} \tag{96}$$

using

$$J \approx \begin{bmatrix} (1-n\Omega_z)\cos\chi & (n\Omega_z-1)\sin\chi \\ \sin\chi & \cos\chi \end{bmatrix} \quad \text{and} \quad II \approx \frac{1}{1-n\Omega_z}\begin{bmatrix} -\Omega_y & \Omega_x \\ \Omega_x & 0 \end{bmatrix}. \tag{97}$$

If we now take the case that the car is travelling straight along the centre line we obtain

$$\begin{bmatrix} \omega_x^b \\ \omega_y^b \end{bmatrix} = \dot{s}\begin{bmatrix} \cos\chi & \sin\chi \\ -\sin\chi & \cos\chi \end{bmatrix}\begin{bmatrix} \Omega_x \\ \Omega_y \end{bmatrix}, \tag{98}$$

which is (18).

We conclude with some comparative calculations for a particular car on the Darlington NASCAR oval, which was selected for its demanding topographic properties. The results resented were all computed using the optimal control package GPOPS II [27]. As in [20], the computed simulations will be compared with results from an industrial simulation tool,

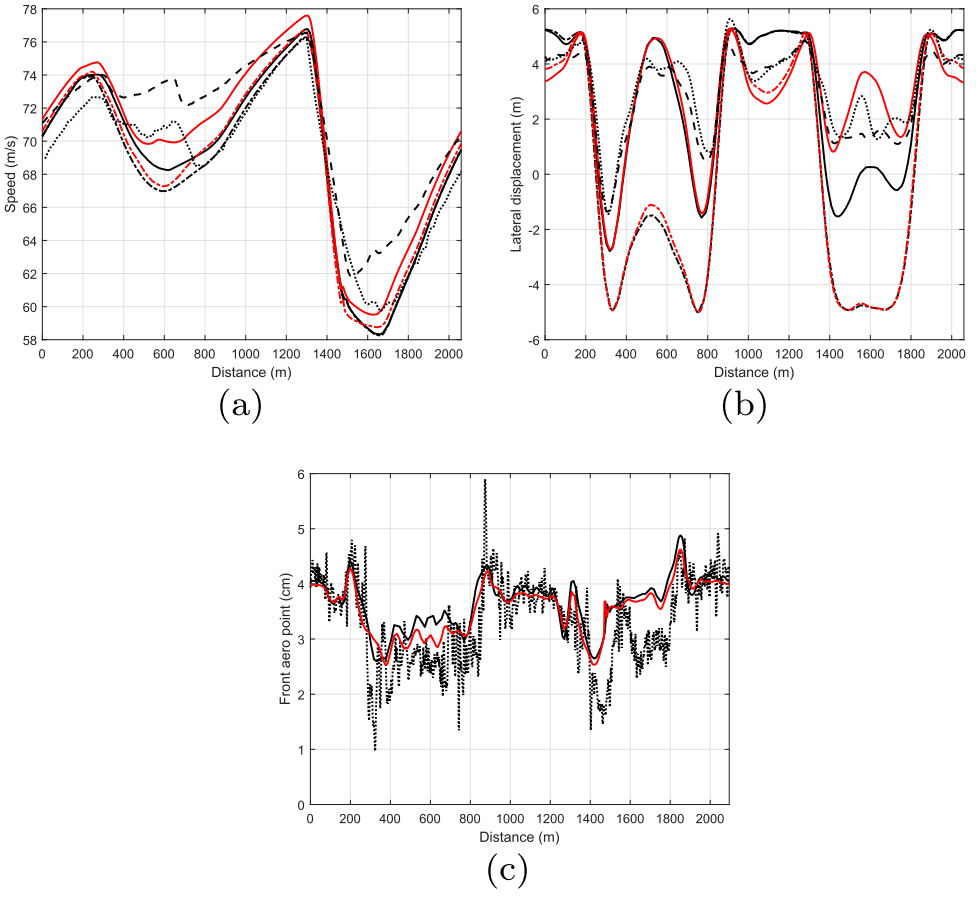


Figure 9. Comparisons of: (a) Vehicle speed. (b) Lateral displacement. (c) Splitter height as a function of the distance travelled.

measured telemetry data captured during a race, and track models using both laterally flat ($m(s,n) = 0$) and laterally curved ($m(s,n) \neq 0$) track models. Following the convention is used: (i) the results computed using the models given in Section 5 will be shown solid red; (ii) the results computed using the models given in Section 7 will be shown solid black; (iii) the results computed using the models given in Section 5 with $m(s,n) = 0$ will be shown dot-dashed red; (iv) the results computed using the models given in Section 7 with $m(s,n) = 0$ will be shown dot-dashed black; (v) the industrial simulation results will be shown black dotted; (vi) some measured race results will be shown black dashed.

Figure 9 shows the car's speed, its offset from the centre line and the height of the front splitter that is used to inform the aerodynamics model. The speed predictions associated with the track models given in Sections 5 and 7 are within 2 m/s throughout a racing lap. For the most part these predictions lie between the measured data and the high-fidelity industrial simulation. In the case that $m(s,n) = 0$, the predictions made by the models in Sections 5 and 7 are comparable and less 'spread out' than in the $m(s,n) \neq 0$ case. In the $m(s,n) = 0$ case the lateral offset predictions made by the models in Sections 5 and 7 are almost identical, but incorrect because they ignore that lateral camber variations of the

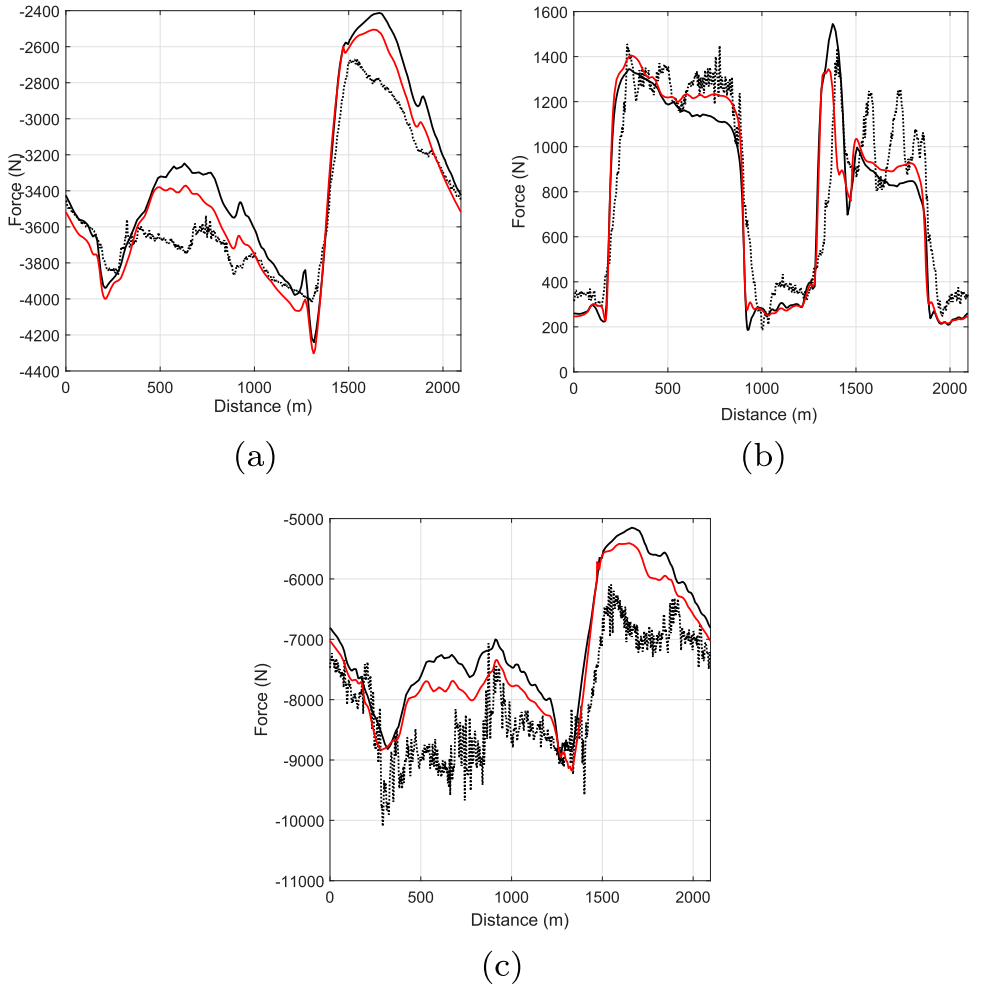


Figure 10. Comparisons of predictions for: (a) Aero drag force. (b) Aero side force. (c) Aero down force as a function of the distance travelled.

track. In the $m(s, n) \neq 0$ case, the predictions are again almost identical for the first 1400 m, with a peak difference of approximately 4 m appearing at 1600 m. At 1600 m the measured and industrial simulation results lie between the two. In this case the Section 5 model appears more accurate. The splitter height predictions made by the two models were in close agreement with each other, and with the prediction made by the industrial simulator.

The aerodynamic force predictions are compared in Figure 10. These prediction use aerodynamic coefficients that are functions of the car's roll and side-slip angles, as well as front- and rear ride heights. If the industrial simulator is taken as reference, the predictions made by the model in Section 5 is to be preferred, but this is in no sense a general conclusion.

The lap times for all the simulations and the measured lap time were between 29.78 s and 30.63 s. The predictions made by the models in Sections 5 and 7 are in generally good agreement.

Table 2. Velocity constraints and the yaw rate equations.

Model type	Translational	Rotational	Yaw rate
2D model	(15)	$\omega_x^b = \omega_y^b = 0$	(13)
3D ribbon model	(15)	(18)	(13)
3D curved-ribbon model	(38) and (39)	(41)	(41)
3D fundamental forms	(75)	(80)	(86)

9. Conclusions

The aim of this paper is to review the road models currently used in vehicular control studies. These include minimum-lap-time optimal control, reference trajectory generation for autonomous vehicles, autonomous racing, real-time MPC-based control algorithms, control studies for vehicles operating under rally-type conditions, drivetrain configuration optimisation, and automated safety systems. These studies have thus far been dominated by simple flat-road models that require minimal mathematical sophistication.

In the last decade 3D road models have attracted growing interest. These have been related predominantly to closed-circuit car and motorcycle racing, but applications in vehicle stability control systems have also emerged. Entry-level 3D road models pertain to inclined planar surfaces, which amount essentially to changing the orientation of the gravity vector. After that ribbon-based road models emerged that treat the road as 'laterally flat'. Motivated be track-modelling issues that emerged from NASCAR racing, these models were subsequently extended to cover cases in which lateral curvature variations are required.

Road models are used to eliminate three of the six freedoms that would normally be associated with airborne vehicles. In the case of car models without a suspension system, these models are used to eliminate the car's vertical translational degree of freedom, as well as its pitch and roll freedoms. When the car has a suspension, a road model is used to constrain the tyre ground-contact kinematics. The translational and rotational constraints associated with the road models studied here are summarised in Table 2.

Road models dealing with lateral curvature variations are not required for most Formula One and NASCAR tracks. As much of the literature suggests, this is also true in many other (non-racing) applications – in many instances even simple flat-road models suffice.

In the case of the Darlington oval for instance, lateral curvature variations have a significant impact on the optimal racing line, the tyre loading and the consequent lap times. The optimal line at Darlington (for typical track grip levels) is for the car to run against the wall for the second half of the track. Most professional drivers run this line with some brushing the wall creating what is called the 'Darlington Stripe', which is evident on both car and wall. As seen in the minimum-time optimal control studies that do not take into account the track's lateral curvature variations, a racing line around the bottom of the track is achieved that is not representative of reality. In this type of 'limit performance' study, the optimal line is dependent on the car's configuration and tyre grip levels under varying temperature and states of wear. In these cases, the entire track surface has to be modelled using detailed survey data and then tuned for purpose. This tuning process could involve the selective removal of several 'small' terms that serve only to increase computation times. Going forward, the modelling challenges associated with high-performance

car and motorcycle OCPs are likely to focus on tyre and aerodynamic modelling that will require accurate road-surface models.

Notes

1. We alert the reader to the fact that u is often used as a body-fixed velocity component in a mechanics setting, while also being standard notion for the control input in a control systems setting. In the same way x may be a position component in a mechanics setting, while possibly representing a state variable in a control systems setting. This said, the context should resolve any ambiguity that might arise.
2. The *first fundamental form* is a symmetric bilinear form $I_P(U, V)$ on the plane T_PM tangent to the road surface M at point $\boldsymbol{x}_P$. It follows from (69) that the square of the car's velocity is

$$(\frac{\mathrm{d}}{\mathrm{d}t}\boldsymbol{x}_P).(\frac{\mathrm{d}}{\mathrm{d}t}\boldsymbol{x}_P) = \begin{bmatrix} \dot{s} & \dot{n} \end{bmatrix} \begin{bmatrix} \partial_s\boldsymbol{x}_P.\partial_s\boldsymbol{x}_P & \partial_s\boldsymbol{x}_P.\partial_n\boldsymbol{x}_P \\ \partial_s\boldsymbol{x}_P.\partial_n\boldsymbol{x}_P & \partial_n\boldsymbol{x}_P.\partial_n\boldsymbol{x}_P \end{bmatrix} \begin{bmatrix} \dot{s} \\ \dot{n} \end{bmatrix}$$

   so that

$$l = \int_a^b \left(\sqrt{\begin{bmatrix} \dot{s} & \dot{n} \end{bmatrix} (I) \begin{bmatrix} \dot{s} \\ \dot{n} \end{bmatrix}} \right) \mathrm{d}t,$$

   is the length of the path travelled.
3. The second fundamental form is used to measure the way in which the road surface 'bends away' from the tangent plane T_PM at $\boldsymbol{x}_P$. The *normal curvature* of the road surface at a point $\boldsymbol{x}_P$ measures its curvature in direction U in the tangent plane, and is defined as

$$\kappa_n(U) = \frac{\Pi_P(U,U)}{U.U} = \frac{\begin{bmatrix} \dot{s} & \dot{n} \end{bmatrix} \Pi_P \begin{bmatrix} \dot{s} \\ \dot{n} \end{bmatrix}}{\begin{bmatrix} \dot{s} & \dot{n} \end{bmatrix} I_P \begin{bmatrix} \dot{s} \\ \dot{n} \end{bmatrix}} = \frac{\begin{bmatrix} \alpha & \beta \end{bmatrix} Q^{-1}\Pi_P Q^{-T} \begin{bmatrix} \alpha \\ \beta \end{bmatrix}}{\alpha^2+\beta^2},$$

   where $I_P = QQ^T$ (I_P is positive definite) and $\begin{bmatrix} \alpha & \beta \end{bmatrix} = \begin{bmatrix} \dot{s} & \dot{n} \end{bmatrix} Q$. On a smooth surface, the normal curvature varies continuously with the direction of U, and ranges between the principal curvatures κ_1 and κ_2 at $\boldsymbol{x}_P$; since $Q^{-1}\Pi_P Q^{-T}$ is symmetric, κ_1 and κ_2 are real (and of either sign).
4. A Taylor series expansion around $n = 0$ is

$$\sqrt{n^2\Omega_x^2 + (1-n\Omega_z)^2} = 1 - n\Omega_z + \frac{n^2\Omega_x^2}{2} + \frac{n^3}{2}\Omega_x^2\Omega_z + \mathcal{O}(n^4).$$

Disclosure statement

No potential conflict of interest was reported by the author(s).

ORCID

D. J. N. Limebeer http://orcid.org/0000-0002-3504-6290

References

[1] Limebeer DJN, Massaro M. Dynamics and optimal control of road vehicles. Oxford, Oxfordshire: Oxford University Press; 2018.
[2] Massaro M, Limebeer DJN. Minimum-lap-time optimization and simulation. Veh Syst Dyn. 2021;59(7):1069–1113.doi:10.1080/00423114.2021.1910718.
[3] Micaelli A, Samson C. Trajectory tracking for unicycle-type and two-steering-wheels mobile robots. Sophia-Antipolis: Inria; 1993. (Research Report RR; 2097).

[4] Timings JP, Cole DJ. Vehicle trajectory linearisation to enable efficient optimisation of the constant speed racing line. Veh Syst Dyn. 2012;50(6):883–901.
[5] Kong J, Pfeiffer M, Schildbach G, et al. Kinematic and dynamic vehicle models for autonomous driving control design. 2015 IEEE Intelligent Vehicles Symposium (IV); 2015 Jun 28-Jul 1; COEX, Seoul, Korea. IEEE; 2015. p. 1094–1099.
[6] Xu W, Wei J, Dolan JM, et al. A real-time motion planner with trajectory optimization for autonomous vehicles. In IEEE International Conference on Robotics and Automation; 2012. p. 2061–2067.
[7] Tavernini D, Massaro M, Velenis E, et al. Minimum time cornering: the effect of road surface and car transmission layout. Veh Syst Dyn. 2013;51(10):1533–1547.
[8] Tavernini D, Velenis E, Lot R, et al. The optimality of the handbrake cornering technique. J Dyn Sys Meas Control. 2014;136:041019–1–041019–11.
[9] Murray RM, Rathinam M, Sluis W. Differential flatness of mechanical control systems: A catalog of prototype systems. In Proceedings of the 1995 ASME International Engineering Congress and Exposition; San Francisco. ASME; 1995. p 12–17.
[10] Scacchioli A, Lu J. Flatness-based electronic posture control (EPC) for accident avoidance. In 2012 American Control Conference; 2012 Jun 27–29; Montréal, Canada. IEEE; 2012. p. 2114–2119.
[11] Liniger A, Lygeros J. A noncooperative game approach to autonomous racing. IEEE Trans Control Syst Technol. 2020;28(3):884–897.
[12] Tseng HE. Dynamic estimation of road bank angle. Veh Syst Dyn. 2001;36(4–5):307–328.
[13] Cui L, Dai JS. A Darboux-frame-based formulation of spin-rolling motion of rigid objects with point contact. IEEE Trans Robot. 2010;26(2):383–388.
[14] Cossalter V, Da Lio M, Lot R, et al. A general method for the evaluation of vehicle manoeuvrability with special emphasis on motorcycles. Veh Syst Dyn. 1999;31(2):113–135.
[15] Perantoni G, Limebeer DJN. Optimal control of a formula one car with variable parameters. Veh Syst Dyn. 2014;52(5):653–678.
[16] Perantoni G, Limebeer DJN. Optimal control of a formula one car on a three-dimensional track. Part 1: Track modelling and identification. ASME J Dyn Sys Meas Control. 2015;137(5):051018. doi:10.1115/1.4028253.
[17] Lot R, Biral F. A curvilinear abscissa approach for the lap time optimization of racing vehicles. In Proceedings of the 19th IFAC World Congress; Cape Town, South Africa; 2014. p. 7559–7565.
[18] Fork T, Tseng HE, Borrelli F. Models and predictive control for nonplanar vehicle navigation. 2021. https://arxiv.org/abs/2104.08427.
[19] Lovato S, Massaro M, Limebeer DJ.N. Curved-ribbon-based track modelling for minimum lap-time optimisation. Meccanica. 2021;56:2139–2152.
[20] Limebeer DJN, Bastin M, Warren E, et al. Optimal control of a nascar–specification race car. Veh Syst Dyn. 2022; 1–26. doi:10.1080/00423114.2022.2067573.
[21] Casanova D, Sharp RS, Symonds P. Technical note: construction of race circuit geometry from on-car measurements. Proc Inst Mech Eng D J Automob Eng. 2001;215(9):1033–1042.
[22] Arnold VI. Mathematical methods of classical mechanics. 2nd ed. New York: Springer; 1989.
[23] Struik DJ. Lectures on classical differential geometry. 2nd ed. New York: Dover; 1961.
[24] Kreyszig E. Differential geometry. 1st ed. New York: Dover; 1991.
[25] do Carmo MP. Differential geometry of curves and surfaces. Englewood Cliffs, NJ: Prentice-Hall; 1976.
[26] Limebeer DJN, Perantoni G. Optimal control of a formula one car on a three-dimensional track part 2: optimal control. ASME J Dyn Syst Meas Control. 2015;137(5):Article ID 051019.
[27] Rao AV, Benson DA, Darby C, et al. GPOPS II: A MATLAB software for solving multiple-phase optimal control problems using hp-adaptive gaussian quadrature collocation methods and sparse nonlinear programming. ACM Trans Math Softw. 2010;37(2):1–39.